Climatology of the Equatorial Thermospheric Mass Density Anomaly

Huixin Liu

Earth and Planetary Science Division, Hokkaido University, Japan

Hermann Lühr

GeoForschungZentrum Potsdam, Potsdam, Germany

Shigeto Watanabe

Earth and Planetary Science Division, Hokkaido University, Japan

Abstract.

The equatorial anomaly is an interesting and important feature of the Earth's thermosphere-ionosphere coupling in tropical regions. It is an anomalous latitudinal distribution found in both the ionized and unionized part of the atmosphere. Its equinox configuration consists of a minimum near the dip equator flanked by two maxima on both sides. The ionospheric side of this anomaly, often referred to as equatorial ionization anomaly (EIA), has long been recognized since the 1930s. However, its thermospheric counterpart was only to be glimpsed by the Dynamic Explorer 2 satellite in the 1970s. A global picture of it has been rather recently revealed by the CHAMP satellite in 2005. In this paper, we complement previous studies by investigating the climatology of the equatorial mass anomaly (EMA) in the thermosphere using 4 years of CHAMP measurements. Our analysis has revealed strong variation of the EMA with season and solar flux level. The EMA structure is most prominent around equinox, with a crest-to-trough ratio about 1.05 for F10.7=150. Near solstices, it is asymmetric about the dip equator. The density crest attains maximum 1–2 hrs earlier and reaches higher values in the summer hemisphere than in the winter hemisphere. The density in EMA regions varies semiannually, with maxima near equinoxes. The latitudinal locations of the EMA crests undergo a seasonal variation, obviously following the movement of the sub-solar point. The EMA structure has also been found to become more pronounced at higher solar flux levels. Both the location and magnitude of the EMA crests closely follow those of the EIA in corresponding seasons and solar flux levels, hence demonstrating strong plasma-neutral interaction. Furthermore, two seasonal asymmetries clearly present in the globally averaged density, with the density in March/December being $\sim 15-20\%$ higher than that in September/June.

1. Introduction

The Earth's thermosphere has been known to be coupled with the ionosphere. Among various features, the equatorial anomaly is a very interesting and important one, revealing strong neutral-plasma interaction. This anomaly, whose equinox configuration shows a minimum near the dip equator flanked by two maxima on both sides, has long been recognized in the ionospheric electron density and referred to as the Appleton anomaly or the Equatorial Ionization Anomaly (EIA). Its formation has been attributed to a fountain effect, mainly driven by the large-scale eastward electric field at low latitudes [e.g. see review of *Rishbeth*, 2000, and references therein]. A similar anomaly has been identified in the thermosphere as well, first in the composition N_2 [*Philbrick and McIsaac*, 1972; *Hedin and Mayr*, 1973], then in the neutral temperature and wind [*Raghavarao et al.*, 1991, 1993], and recently in the total air mass density [*Liu et al.*, 2005]. These anomalous latitudinal distributions in both the ionized and unionized part of the atmosphere demonstrate the strong ionosphere-thermosphere coupling at low and middle latitudes.

The EIA structure has been investigated extensively in the past, and its morphology is now largely known [e.g. *Thomas*, 1968; *Sharma and Hewens*, 1976; *Walker et al.*, 1994; *Huang and Cheng*, 1996; *Tsai et al.*, 2001; *Liu and Wan*, 2001; *Liu et al.*, 2006b]. In contrast, its thermospheric counterpart has so far lacked sufficient study. This may partly be due to the fact that neutral particles are more difficult to probe than the charged ones. *Mayr et al.* [1974] briefly discussed the anomaly in individual atmospheric compositions around equinox and June solstice using a numerical model. The two density crests of this anomalous structure were shown to be asymmetric at June solstice, with higher density in the winter hemisphere. However, these predictions and proposed mechanisms have so far not been validated by observations. Utilizing one year observations from the satellite CHAMP, *Liu et al.* [2005] obtained a global picture of the equatorial air mass density anomaly (abbreviated as EMA in the following). This EMA structure has been observed to generally appear after 10 local time (LT) and persists till $\sim$ 19–21 LT depending on season, being most prominent between 11–16 LT. Its formation was speculated to be caused by ion drag and charge-exchange released chemical heating, both of which are related to the EIA structure. However, this hypothesis could not be examined from a climatological point of view due to limited data. In addition, the Mass Spectrometer Incoherent Scatter (MSIS) model [*Hedin et al.*, 1991], which is widely used for satellite orbital predictions, is currently unable to reproduce the EMA structure either [*Liu et al.*, 2005]. Therefore, further studies clarifying the climatology of the equatorial thermospheric anomaly are highly needed for both theoretical and practical purposes. As a following-up study of *Liu et al.* [2005], we investigate in this pa-

0148-0227/07/$9.00

per the EMA variations with season, geomagnetic activity and solar flux levels by using 4 years of CHAMP measurements during 2002–2005. Given the hypothesis of *Liu et al.* [2005], we would expect these EMA climatological variations to closely follow those of the EIA.

2. Methodology and Data Selection

The CHAMP satellite was launched on July 15, 2000 into a near-circular orbit with an inclination of 87.3° and an initial altitude of 456 km. The precessing rate of its orbital plane is $\sim 1.5^\circ$/day. Among various scientific instruments onboard, a tri-axial accelerometer effectively probes the in-situ air drag, which yields estimates of the air mass density with an accuracy of 1×10^{-14} kg m^{-3} at a sample rate of 0.1 Hz (Level 2 data). The detailed procedure for deriving the mass density from the CHAMP accelerometer has been described in *Liu et al.* [2006a]. It improves the one given in *Liu et al.* [2005] by effectively removing the influence of cross-track wind on the derived density. In the present study, we use measurements during 11–16 LT, where the EMA structure is most prominent. These data are further classified into "quiet" (Kp$\leq$ 2) and "moderate" (3 $\leq$Kp$\leq$ 4+) geomagnetic conditions (the current 3-hour Kp values are used). Very active periods with Kp$\geq$ 5 are not analyzed due to possibly increasing error from in-track winds and limited number of samples. The monthly mean is then obtained for each activity level by averaging densities falling into the 11-16 LT sector during each calendar month, for every 3 degrees in corrected geomagnetic (cgm) latitudes. By doing so, we ignore the relatively small local time variation around noon and focus on the long-term variations with season and solar cycle. The number of satellite passes contributing to the average of each month at the equator is shown in Figure 1. Owing to CHAMP's high inclination of 87.3°, the number of passes varies little with latitudes within $\pm60^\circ$. Density variations due to changes in orbital altitude have been removed before the averaging, via a normalization to a common altitude of 400 km using the NRLMSIS model [*Picone et al.*, 2002]. Since CHAMP's mean altitude at low and middle latitudes varied within 412–360 km during the years of 2002–2005 (see Figure 1), the normalization was applied within one scale height. Therefore, errors caused by this procedure are expected to be small (within 5% given a similar uncertainty in the MSIS predicted scale height) and will not seriously compromise the EMA climatology discussed below.

3. Longitudinal Variation of the Thermospheric Mass Density

Figure 2 depicts the noon-time mass density distribution in geographic coordinates at 400 km altitude, averaged over calendar months of February–April. Density variations due to solar flux levels have been removed by normalizing all density to a fix solar flux level of $F10.7 = 150 \times 10^{-22}$ W m^{-2} Hz^{-1} using the NRLMSIS model (the "observed" values of F10.7 were used during this procedure). The high density bands on both sides of the equator, sandwiching a shallow minimum in between can be clearly recognized. In particular, these bands are well aligned with the dip equator, which is indicated by the black line in the figure. This alignment clearly demonstrates that the EMA structure is magnetically controlled. Consequently, in geographic coordinates, the density experiences a strong longitudinal variation, particularly in the -90°–0° longitude sector. However, when discussed in geomagnetic coordinates, the longitudinal variation becomes less significant. Therefore, we discuss in the following sections the climatology of the longitudinally averaged EMA structures in geomagnetic coordinates.

4. Climatological Variations

Figure 3 presents the mass density variation with geomagnetic latitude and month of the year for two different geomagnetic activity levels at a fixed solar flux level of F10.7=150. The black lines depict the locations of the density peaks in corresponding hemispheres. The x-axis represents month of the year, with January from 0–1, February from 1–2, etc. The interval of 12–13 is a repetition of January, plotted here to show the density structure in December and January more clearly. The seasonal mean of the EMA structures are obtained by averaging corresponding months and shown in Figure 4. These figures reveal the seasonal and geomagnetic activity variations of the EMA as described below. The words "spring", "summer", "autumn", and "winter" mean local seasons.

4.1. Seasonal Variations under Quiet Conditions

Main features emerged from the top panels of Figures 3 and 4 under quiet conditions can be summarized as follows. (1) It is immediately evident that the EMA structure is most pronounced around equinoxes, with two well-defined density crests. The crest-to-trough ratio reaches a value of $\sim$ 1.05. Near solstices, it is asymmetric about the dip equator as expected (better seen in Figure 4). Both crests shift towards the summer hemisphere by about 10°–15° in latitudes, with higher densities in the summer hemisphere than in the winter hemisphere. (2) The density in EMA regions varies semiannually, with maxima near equinoxes. However, it is notable that the density in September–October peaks about one month after the September equinox (see upper panel in Figure 3), in agreement with previous observations [e.g. *King-Hele and Walker*, 1969; *Moore*, 1983]. A similar delay has also been recognized in the electron density [*Balan et al.*, 1998]. (3) The locations of the EMA crests (indicated as black lines in Figure 3) undergoes a seasonal variation, obviously following the movement of the sub-solar point. Both crests move significantly equatorward in local winter. They are located near $\pm15^\circ$ cgm latitudes in winter, around $\pm25^\circ$ cgm latitude in spring and autumn, and beyond $\pm30^\circ$ in summer.

Furthermore, two asymmetries are clearly discernible. First, an apparent asymmetry exists between the two equinoxes in magnitudes of the mass density at all latitudes. The mean density around March equinox is about $7-10\%$ higher than that around September equinox. Second, a June-December asymmetry can be clearly seen at all latitudes below 40°, with ρ in December exceeding ρ in June by a factor of 1.2 in equatorial regions. This asymmetry consequently leads to a winter anomaly in the northern EMA crest, but not in the southern crest. When averaged over all latitudes, the thermospheric density near December solstice is larger than near June solstice, being respectively 6.18×10^{-12} kg m^{-3} and 5.33×10^{-12} kg m^{-3}. Therefore, a June/December asymmetry exists in the globally averaged thermospheric density, with an asymmetry index of 0.074 when defined as $\frac{Dec-June}{Dec+June}$ [*Mendillo et al.*, 2005; *Zhao et al.*, 2005]. This is consistent with the satellite orbit analysis by *King-Hele and Walker* [1969] and *Boulton* [1985], which revealed ρ in December being over 1.3 times of that in June within the altitude of 240–470 km. This corresponds to an asymmetry index of about 0.13, which is higher than 0.074 observed by CHAMP near 400 km height. Given the altitude difference, their larger asymmetry index may indicate possible deepening of the June-December asymmetry at lower altitudes. We therefore may speculate that influences from below (i.e., lower atmosphere) could play a role in the formation of this annual anomaly.

4.2. Seasonal Variation under Disturbed Conditions

In comparison to quiet conditions, the density increases under disturbed conditions as seen in the 2nd panels of Figures 3 and 4. But the seasonal variation of EMA remains similar, with semiannual variation and June-December asymmetry. Two new features to note include: (1) the equinox asymmetry grows stronger as better seen in the lower panel of Figure 4, with the density around March equinox (ME) about $15\%-20\%$ higher than that around September equinox (SE). This leads to an asymmetry index of about 0.07 when defined in a similar manner as for the solstice, being $\frac{ME-SE}{ME+SE}$; (2)

the density maximum in September–October seems to peak at earlier time with increasing geomagnetic levels, being near the end of September under disturbed time in comparison to October under quiet conditions.

4.3. The Solar Flux Variation

The EMA structure has also been found to become more pronounced at higher solar flux levels. An example is shown in Figure 5 for equinoxes case. It presents the average EMA profile at three different F10.7 levels. The number of contributing satellite passes for each F10.7 level are 875, 1054, and 594, respectively. Note that the y-axis range in each plot has been adjusted to show the latitudinal variation more clearly, but the scale remains the same. It is not difficult to notice that in addition to the general increase of the density with increasing F10.7 at all latitudes, the EMA double-hump structure becomes more distinct at higher F10.7 levels. The crest-to-trough difference increases from about 0.1×10^{-12} kg m^{-3} for $F10.7 < 100$ to over 0.4×10^{-12} kg m^{-3} for $150 \leq F10.7 \leq 200$. In addition, there is a trend for the EMA crests to move poleward with increasing F10.7. For instance, the crest center shifts from about $\pm 20^{\circ}$ for $F10.7 < 100$ to $\pm 25^{\circ}$ for $150 \leq F10.7 \leq 200$. Accompanying these changes in the EMA, the EIA structure varies in a similar manner as reflected in the electron density observed by CHAMP in corresponding conditions. The EIA structure grows more pronounced, with the crest-to-trough ratio increasing from ~ 1.16 to ~ 1.24. The crest center also moved poleward, from $\pm 10^{\circ}$ for $F10.7 < 100$ to $\pm 15^{\circ}$ for $150 \leq F10.7 \leq 200$.

5. Discussion

The above analysis of 4 years of CHAMP observations has reconfirmed many previously reported thermospheric features, like the semiannual variation and June-December asymmetry [e.g. *Boulton*, 1985; *Jacchia and Slowey*, 1968; *King-Hele and Walker*, 1969; *Moore*, 1983]. Furthermore, it has revealed valuable climatological features of the EMA, which could not be examined before due to limited observations. In the following, we compare these features with those predicted by numerical models or seen in the EIA, which is the ionospheric counterpart of the EMA.

5.1. Comparison with Model Predictions

Among various numerical models, the one by *Mayr et al.* [1974] seems to be the only reported model to be able to produce an equatorial anomaly in the thermosphere. Therefore, it is interesting to compare their predictions with the CHAMP observations presented above. Their model predicted an equatorial anomaly near 450 km altitude, which was obvious in the atmospheric composition of $[N_2]$, and weakly discernible in $[O]$. This anomalous structure was shown to be symmetric about the equator around equinox and asymmetric at June solstice, with higher density in the winter hemisphere. Since the atmosphere is dominated by $[O]$ and $[N_2]$ at altitudes above about 350 km, these structures in the composition should result in similar structures in the total mass density which can be approximated by $16[O] + 28[N_2]$. Comparing with the total mass density observed by CHAMP, we immediately notice the discrepancy between the prediction and observations at June solstice. The hemispheric asymmetry in the individual composition shown by the model leads to a higher total mass density in the winter hemisphere than in the summer hemisphere. However, CHAMP has observed the opposite, with higher density in the summer hemisphere (see Figure 4).

Furthermore, the model of *Mayr et al.* [1974] predicted a LT shift between the two density crests in two hemispheres at solstice, with the one in the winter hemisphere occurring 1–2 hrs earlier in LT than that in the summer hemisphere. To examine this feature, contour plots of the CHAMP observed density distribution over LT and geographic latitudes are presented in Figure 6. We see two EMA crests, which are at similar LT near equinoxes but phase-shifted near solstices. The EMA crest in the summer hemisphere tends to occur 1–2 hrs earlier than that in the winter hemisphere. This tendency in LT shift apparently disagrees with that predicted by the model. Therefore, the CHAMP observations do not seem to support the model predictions.

5.2. Comparison with Seasonal and Solar Flux Variation of EIA

The CHAMP observations have shown strong seasonal variations of the EMA structure. In particular, the locations of the EMA crests move poleward in local summer and equatorward in local winter, following the movement of the subsolar point. The EMA northern crest experiences a winter anomaly which does not exist in the southern crest. The thermospheric anomalies mentioned in the introduction have been speculated to be caused by the EIA [*Hedin and Mayr*, 1973; *Raghavarao et al.*, 1991; *Liu et al.*, 2005]. Given this hypothesis, we would expect the climatological variation of the EMA to closely follow that of the EIA, particularly its location and magnitude. In the following, we examine this speculation by comparing with the seasonal and solar flux variations of the EIA.

The seasonal variation of EIA has been extensively investigated in many studies [e.g. *Thomas*, 1968; *Sharma and Hewens*, 1976; *Tsai et al.*, 2001; *Liu et al.*, 2006b]. Here we take the results of *Tsai et al.* [2001] about the total electron contents (TEC) for comparison. Using TEC from the Global Positioning System (GPS), they showed that the EIA high density crests move significantly equatorward in local winter, down to about $\pm 9^{\circ}$ geomagnetic latitudes. While in summer, the EIA density crests was found to shift towards higher latitudes. This seasonal movement of the EIA crests agrees well with that of the EMA as seen in Figure 3. *Tsai et al.* [2001] have also showed that the EIA northern crests experience a winter anomaly, but the southern crest does not. The same trend is observed in the EMA (see Figure 4). The EIA structure has also been known to be more pronounced at higher solar flux levels, with the peak-to-trough difference increases [e.g. *Walker et al.*, 1994]. This behavior again resembles the EMA variation with solar flux levels, as seen in Figure 5.

Therefore, both the locations and magnitudes of the EMA crests closely follow those of the EIA in corresponding seasons and solar flux levels. This supports the argument that the EIA could lead to the EMA structure of the neutral atmosphere. The principle physical processes involved are likely to be the ion drag [*Hedin and Mayr*, 1973] and the chemical heating related to charge-exchange process [*Fuller-Rowell et al.*, 1997]. The ion drag, which is larger at the EIA crest latitudes due to higher electron density, slows down the zonal wind hence the transport of energy and mass from the dayside thermosphere towards nightside. This can lead to higher thermospheric mass density in the crest regions. At the same time, chemical heating fueled by the charge-exchange between O^+ and O_2 or N_2 occurs when charged particles fall down along geomagnetic field lines [*Fuller-Rowell et al.*, 1997]. It is especially effective in the E-region and the released energy is equivalent to a radiation at $\lambda = 806$ nm. Consequently, the thermospheric temperature increases and the atmosphere expands correspondingly. Since the footprints of the EIA crests in the E region are at about $\pm 20^{\circ}$ magnetic latitudes, this chemical heating process seems to contribute to the latitudinal offset between EMA and EIA.

Superposed on the ion drag and chemical heating effect, the large-scale meridional wind circulation [e.g. *Roble et al.*, 1987] may also influence the EMA formation. Being usually poleward at day and equatorward at night, the meridional wind may enhance the EMA structure by transporting energy and mass from the equator to middle latitudes at day and suppress it at night by opposite transportation. This regulation may have contributed to the termination of the EMA at night. Interestingly, as shown in Figure 6, the EMA seems to persist longer to $\sim$20/21 LT at equinox, but terminates earlier at solstices ($\sim$17/18 LT). This tendency agrees with the switching time of the meridional wind, which has been found to occur around 20 LT at equinoxes but shift to earlier time at solstices [*Kawamura et al.*, 2000]. However, we cannot evaluate this point

directly here due to the lack of simultaneous meridional wind measurements from the CHAMP satellite. Another mechanism related to heating by precipitated energetic neutral atoms from the radiation belt was proposed by *Tinsley* [1981]. Such precipitation has been shown by *Sorbo et al.* [2006] to peak at the magnetic equator during quiet times, but to develop a second peak away from equator which can reach 35° magnetic latitude in the growth and main phase of magnetic storms. Consequently, if these precipitated neutral particles produce sufficient heating, it would lead to a density maximum at the equator under quiet conditions, and with a second density enhancement on both sides of the equator during magnetic storms. However, since the observed EMA under quiet conditions shows density minimum instead of maximum at the dip equator, such precipitation is unlikely to contribute to the EMA formation. The CHAMP observations thus seem to offer little supporting evidence for this proposed mechanism.

Finally, we would also like to add a few words about the equinox asymmetry in the thermospheric density. As described in section 4.2 and better seen in Figure 4, a clear equinox asymmetry exists in the thermospheric mass density, with higher values in March than in September at all latitudes. A similar trend has been recognized by *Balan et al.* [1998] in the daytime electron density near and above the F region peak using MU radar observations at middle latitudes ($\sim 35^\circ$ N). They attributed this asymmetry to the meridional neutral wind, which was northward but $\sim 40\%$ ($\sim$20 m s^{-1}) weaker near March equinox in comparison to September equinox. This would keep the March equinox HmF2 at a higher altitude where the recombination rate is low, hence leads to higher electron density than at September equinox. Though the related physical processes may differ, we find this difference in the meridional wind may also be invoked to explain the equinox asymmetry in the thermospheric mass density observed by CHAMP. According to the "spoon mechanism" proposed by *Fuller-Rowell* [1998], a stronger meridional wind would lead to a stronger mixing of the atmosphere in September. This would increase the mean molecular mass, resulting in a reduced atmospheric scale height. Consequently, the thermospheric total mass density at a fixed altitude would become smaller in September in comparison to March. This equinox asymmetry has been observed by CHAMP to become stronger at higher geomagnetic activity levels (see Figure 4), hence may indicate a stronger equinox asymmetry in the meridional wind.

In summary, the EMA shows strong variation with season and solar flux levels. It is most prominent around equinox at high solar flux levels. The latitude variations of EMA crests closely follow those of the EIA, hence adding supporting evidence for the important role of EIA in the EMA formation through ion drag and chemical heating. However, previous studies have also shown that unlike the EIA which persists till postmidnight, the EMA structure becomes indiscernible at night [*Liu et al.*, 2005]. This feature seems to apparently deviate from a simple EIA-EMA cause-effect relationship. Superposed on the EIA effect could be the regulation by the meridional wind. Blowing poleward/equatorward at day/night, it could enhance/suppress the EMA structure via meridional transportation and potentially contribute to the EMA termination at night. To reconcile various factors and also to understand their relative importance, simultaneous measurements of the meridional wind would be essential, and diagnostic runs with a coupled thermosphere-ionosphere model is also highly desirable.

Acknowledgments. We thank W. Köhler for processing the CHAMP ACC data and D. Cooke for providing the CHAMP electron density data. The work of H. Liu is supported by the Japanese Society of Promotion of Science (JSPS) foundation. The CHAMP mission is supported by the German Aerospace Center (DRL) in operation and by the Federal Ministry of Education and Research (BMBF) in data processing.

References

Balan, N., Y. Otsuka, G. J. Bailey, and S. Fukao (1998), Equinoctial asymmetries in the ionosphere and thermosphere observed by the MU radar, *J. Geophys. Res.*, *103*, 9481–9495.

Boulton, W. J. (1985), The determination and analysis of the orbit of Nimbus 1 rocket, 1964-52b: the semi-annual variatio in air density from June 1968 to August 1974, *Planet. Space Sci.*, *33*, 1417–1431.

Fuller-Rowell, T. J. (1998), The thermospheric spoon: A mechanism for the semiannual density variation, *J. Geophys. Res.*, *103*, 3951–3956.

Fuller-Rowell, T. J., M. V. Codrescu, B. G. Fejer, W. Borer, F. Marcos, and D. N. Anderson (1997), Dynamics of the low-latitude thermosphere: Quiet and Disturbed conditions, *J. Atmos. Terr. Phys.*, *61*, 1533–1540.

Hedin, A. E., and H. G. Mayr (1973), Magnetic control of the near equatorial neutral thermosphere, *J. Geophys. Res.*, *78*, 1688–1691.

Hedin, A. E., et al. (1991), Revised global model of thermosphere winds using satellite and ground-based observations, *J. Geophys. Res.*, *96*, 7657–7688.

Huang, Y.-N., and M. Cheng (1996), Solar cycle variations of the equatorial ionospheric anomaly in total electron content in the asian region, *J. Geophys. Res.*, *101*, 24,513–24,520.

Jacchia, L. G., and J. W. Slowey (1968), Diurnal and seasonal latitudinal variations in the upper atmosphere, *Planet. Space Sci.*, *16*, 509–524.

Kawamura, S., Y. Otsuka, S.-R. Zhang, S. Fukao, and W. L. Oliver (2000), A climatology of middle and upper atmosphere radar observations of thermospheric winds, *J. Geophys. Res.*, *105*, 12,777–12,788, doi: 10.1029/2000JA900013.

King-Hele, D. G., and D. M. C. Walker (1969), Air density at a height of 470 km between January 1967 and May 1968, from the orbit of the satellite 1966-118A, *Planet. Space Sci.*, *17*, 197–215.

Liu, H., H. Lühr, V. Henize, and W. Köhler (2005), Global distribution of the thermospheric total mass density derived from CHAMP, *J. Geophys. Res.*, *110*, A04301, doi:10.1029/2004JA010741.

Liu, H., H. Lühr, S. Watanabe, W. Köhler, V. Henize, and P. Visser (2006a), Zonal winds in the equatorial upper thermosphere: decomposing the solar flux, geomagnetic activity, and seasonal dependencies, *J. Geophys. Res.*, A09S29, doi:10.1029/2005JA011415.

Liu, L., and W. Wan (2001), The evolution of equatorial trough of ionospheric f-region ionization, *Terr. Atmos. Oceanic Sci.*, *12*, 559–565.

Liu, L., W. Wan, B. Ning, O. M. Pirog, and V. I. Kurkin (2006b), Solar activity variations of the ionospheric peak electron density, *J. Geophys. Res.*, A08304, doi:10.1029/2006JA011598.

Mayr, H. G., A. E. Hedin, C. A. Reber, and G. R. Carignan (1974), Global characteristics in the diurnal variations of the thermospheric temperature and composition, *J. Geophys. Res.*, *79*, 619–628.

Mendillo, M., C.-L. Huang, X. Pi, H. Rishbeth, and R. Meier (2005), The global ionospheric asymmetry in total electron content, *J. Atmos. Solar-Terr. Phys.*, *67*, 1377–1387.

Moore, P. (1983), The semi-annual variation in air density for 1974-1978 from the orbit of 1972-05b, *Planet. Space Sci.*, *31*, 1501–1515.

Philbrick, C. R., and J. P. McIsaac (1972), Measurements of atmospheric composition near 400 km, *Space Research*, *12*, 743–750.

Picone, J. M., A. E. Hedin, D. P. Drob, and A. C. Aikin (2002), NRLMSISE-00 empirical model of the atmosphere: Statistical comparisons and scientific issues, *J. Geophys. Res.*, *107*, 1468, doi: 10.1029/2002JA009430.

Raghavarao, R., L. E. Wharton, N. W. Spencer, H. G. Mayr, and L. H. Brace (1991), An equatorial temperature and wind anomaly (ETWA), *Geophys. Res. Lett.*, *18*(9), 1193–1196.

Raghavarao, R., W. R. Hoegy, N. W. Spencer, and L. E. Wharton (1993), Neutral temperature anomaly in the equatorial thermosphere - a source of vertical winds, *Geophys. Res. Lett.*, *20*(11), 1023–1026.

Rishbeth, H. (2000), The equatorial f-layer: progress and puzzles, *Ann. Geophys.*, *18*, 730–739.

Roble, R. G., E. C. Ridley, and R. E. Dickinson (1987), On the global mean structure of the thermosphere, *J. Geophys. Res.*, *92*, 8745–8758.

Sharma, R. P., and E. J. Hewens (1976), A study of the equatorial anomaly at American longitudes during sunspot minimum, *J. Atmos. Terr. Phys.*, *38*, 475–484.

Sorbo, M., F. Soraas, K. Aarsnes, K. Oksavik, and D. S. Evans (2006), Latitude distribution of vertically precipitating energetic neutral atoms observed at low altitudes, *Geophys. Res. Lett.*, *33*, L06108, doi: 10.1029/2005GL025240.

Thomas, L. (1968), The F2-region equatorial anomaly during solstice periods at sunspot maximum, *J. Atmos. Terr. Phys.*, *30*, 1631–1640.

Tinsley, B. A. (1981), Neutral atom precipitation - a review, *J. Atmos. Terr. Phys.*, *43*, 617–632.

Tsai, H.-F., J.-Y. Liu, W.-H. Tsai, C.-H. Liu, C.-L. Tseng, and C.-C. Wu (2001), Seasonal variations of the ionospheric total electron content in Asian equatorial anomaly regions, *J. Geophys. Res.*, *106*, 30,363–30,369.

Walker, G. O., J. H. K. Ma, and E. Golton (1994), The equatorial ionospheric anomaly in electron content from solar minimum to solar maximum for South East Asia, *Ann. Geophys.*, *12*, 195–209.

Zhao, B., W. Wan, L. Liu, X. Yue, and S. Venkatraman (2005), Statistical characteristics of the total ion density in the topside ionosphere during the period 1996–2004 using empirical orthogonal function (EOF) analysis, *Ann. Geophys.*, *23*, 3615–3631.

H. Liu and S. Watanabe, Earth and Planetary Science Division, Hokkaido University, Sapporo 060-0810, Japan (huixin@ep.sci.hokudai.ac.jp)

H. Lühr, GeoForschungZentrum Potsdam, D-14473 Potsdam, Germany

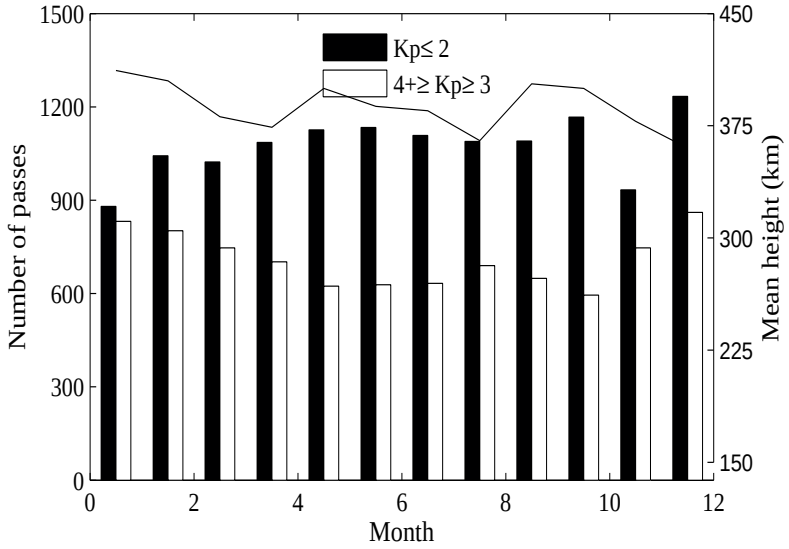

Figure 1. Number of satellite passes contributing to the monthly means in Figure 3 for two different geomagnetic activity levels. The line on the top represents the satellite's mean altitude in corresponding months.

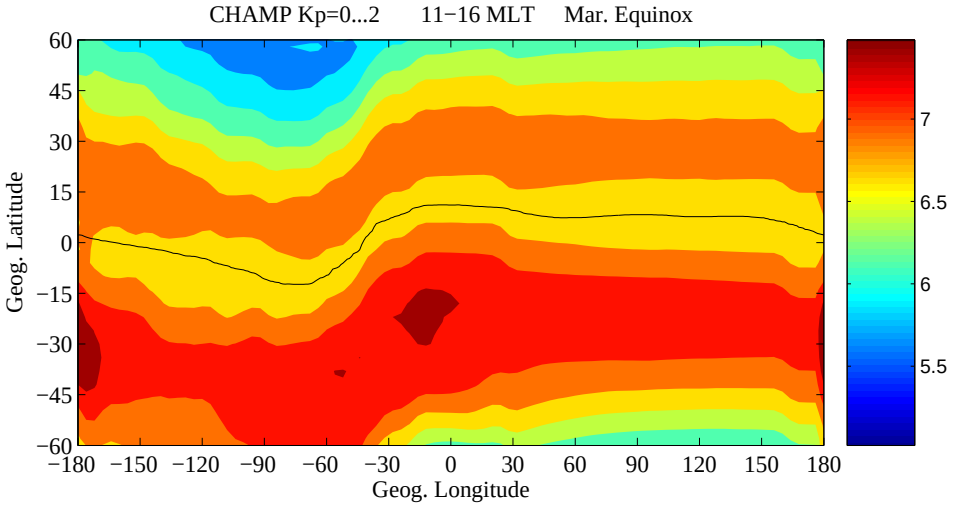

Figure 2. Distribution of the dayside thermospheric mass density (in units of 10^{-12}kg m^{-3}) over geographic coordinates under quiet geomagnetic conditions for a solar flux level of F10.7=150. Smoothing was applied to emphasize only the large-scale variations. The black line indicates the dip equator. Note the high density bands on both sides of the dip equator.

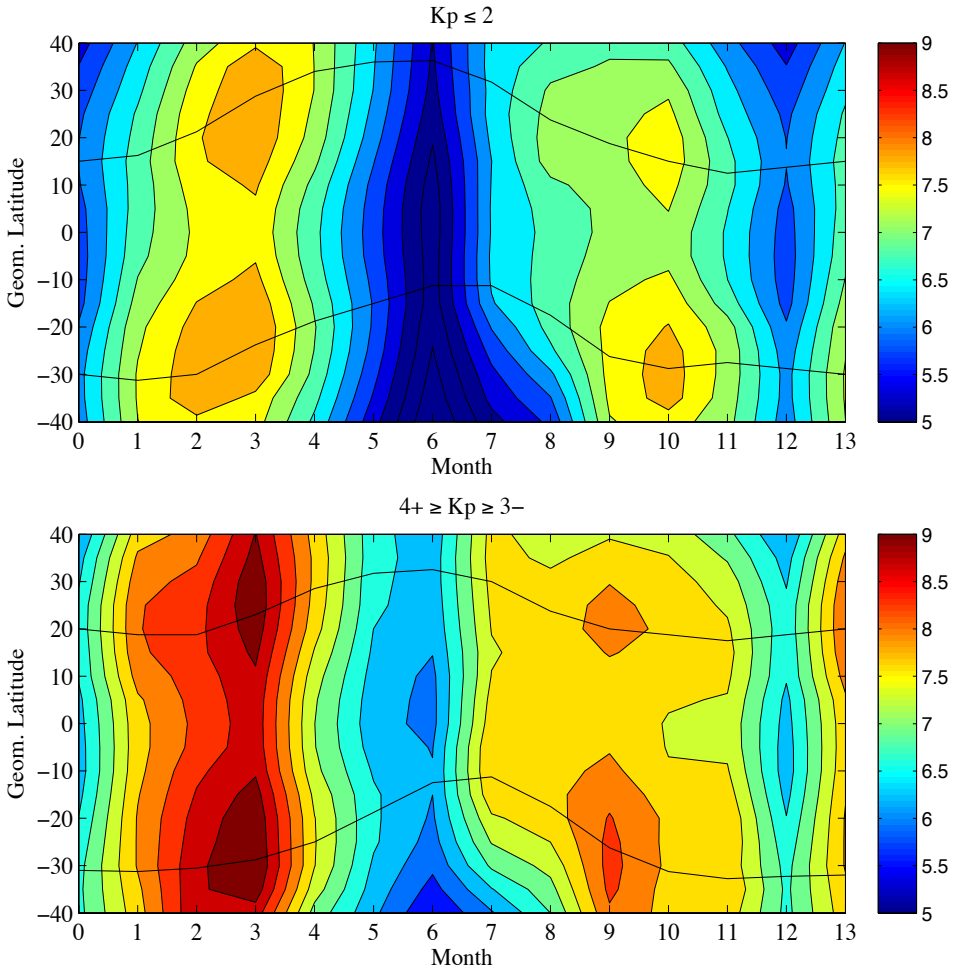

Figure 3. The mass density (in units of 10^{-12}kg m^{-3}) variation with geomagnetic latitude and month of the year at 400 km altitude for a fixed solar flux level of F10.7=150. The black lines depict the locations of the density peaks in corresponding hemispheres. The x-axis represents month of the year, with January from 0–1, February from 1–2, etc. The interval of 12–13 is a repetition of January, making it easier to recognize the density structures in December and January.

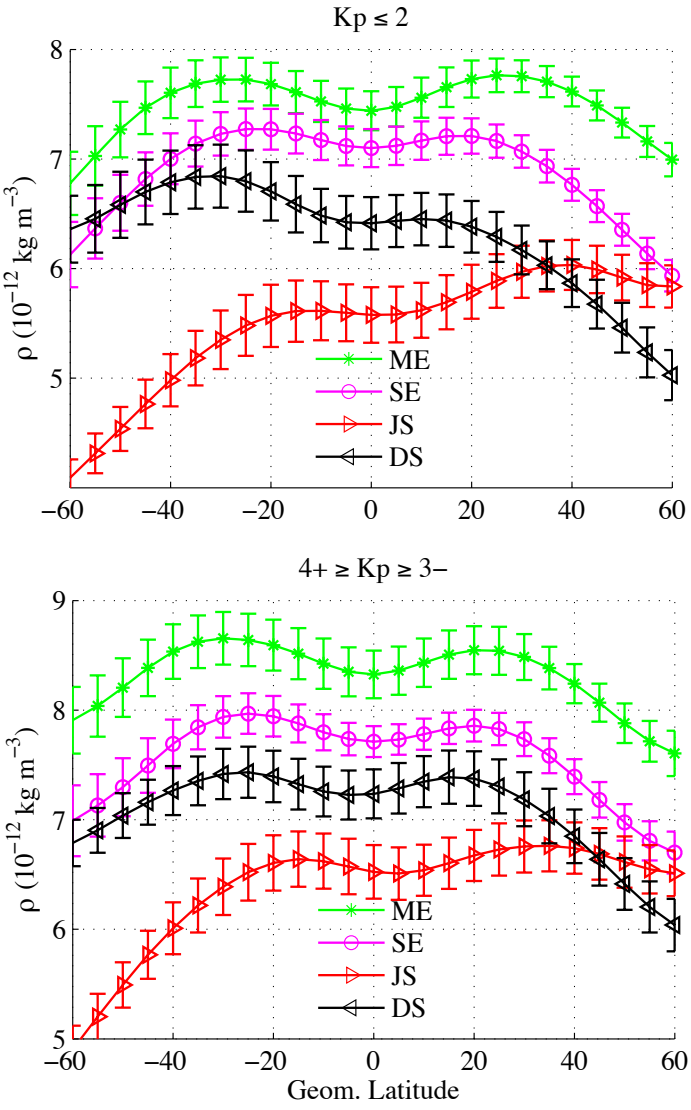

Figure 4. The EMA latitudinal profiles at 400 km altitude for different seasons at a fixed solar flux level of F10.7=150. The profiles are averaged over February–April for March equinox (ME), August–October for September equinox (SE), May–July for June solstice (JS), and November-January for December solstice (DS).

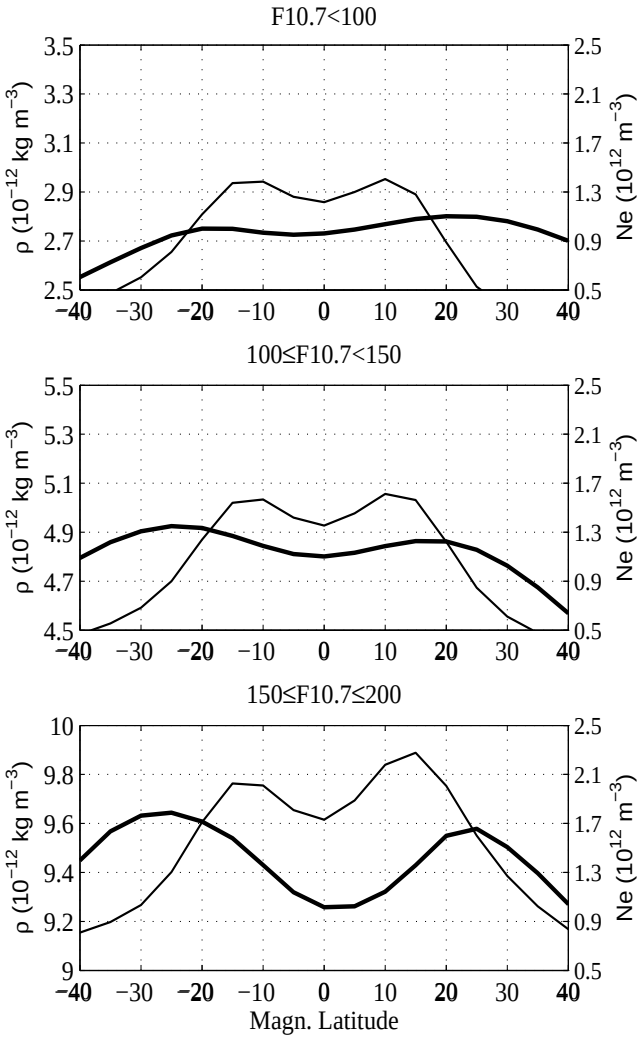

Figure 5. The average latitudinal profiles of the neutral mass density and the electron density at 400 km for different solar flux levels around equinoxes. The profiles are averaged between 11–16 LT. Heavy lines: the neutral mass density; light lines: the electron density. The number of contributing satellite passes for three F10.7 levels are 875, 1054, and 594, respectively.

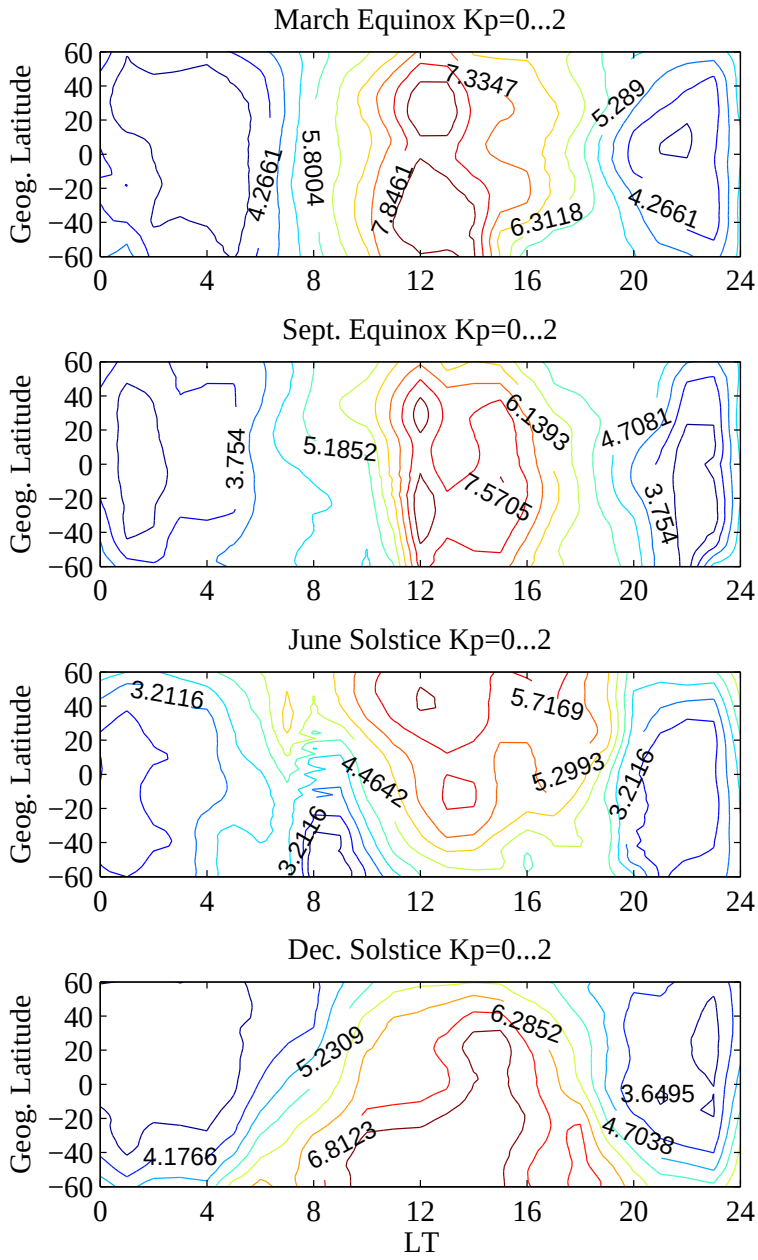

Figure 6. Distribution patterns of the thermospheric total mass density (in units of 10^{-12}kg m^{-3}) over LT and geographic latitudes in different seasons under quiet geomagnetic conditions. A double-hump structure can be recognized after about 10 LT and before about 18–21 LT depending on season.